nature synthesis

Article

https://doi.org/10.1038/s44160-022-00193-3

A general approach to 3D-printed single-atom catalysts

Received: 30 March 2022

Accepted: 13 October 2022

Published online: 2 January 2023

Check for updates

Fangxi Xie[1,7], Xiaolin Cui[2,3,7], Xing Zhi[1,7], Dazhi Yao[1], Bernt Johannessen[4], Ting Lin[5], Junnan Tang[6], Tim B. F. Woodfield[2], Lin Gu[5] & Shi-Zhang Qiao[1]

A mass production route to single-atom catalysts (SACs) is crucial for their end use application. To date, the direct fabrication of SACs via a simple and economic manufacturing route remains a challenge, with current approaches relying on convoluted processes using expensive components. Here, a straightforward and cost-effective three-dimensional (3D) printing approach is developed to fabricate a library of SACs. Despite changing synthetic parameters, including centre transition metal atom, metal loading, coordination environment and spatial geometry, the products show similar atomic dispersion nature of single metal sites, demonstrating the generality of the approach. The 3D-printed SACs exhibited excellent activity and stability in the nitrate reduction reaction. It is expected that this 3D-printing technique can be used as a method for large-scale commercial production of SACs, thus enabling the use of these materials in a broad spectrum of industrial applications.

Single-atom catalysts (SACs) are materials with isolated metal atoms as active sites, anchored by surrounding coordination species of solid supports[1,2]. Advantages include high atom economy and tunable coordination properties, giving potential for numerous applications[3–9]. Developing universal synthesis approaches to achieve scale production of SACs is a prerequisite for successful implementation of these catalysts in practical applications[1]. A simple and economic general synthesis approach for scale production of SACs is vital for downstream commercialization[1,10,11].

Currently, the chemical synthesis strategies of SACs can be divided into two major categories: 'top-down' and 'bottom-up' strategies[1,12–15]. A typical 'top-down' strategy includes the initial creation of defects on substrates and the subsequent anchoring of metal atoms to surface vacancies[13,15–24]. The 'bottom-up' strategy begins with the preparation of host materials, such as microporous crystalline frameworks or synthetic polymers. Afterwards, SACs can be achieved through the confinement of molecular complexes in hosts and subsequent post-integration process to remove the ligands of metal complexes[14,17,25–28]. However, both synthetic strategies require complex wet-chemistry processes, for example the complex defect-construction process or the sophisticated host-material preparation process, hindering scale production of SACs[16,29–34]. In addition, the presence of elaborate substrates and costly precursors (for example, complicated ligands or expensive artificial polymers) notably increases the overall cost of manufacturing SACs[1,35]. Apart from chemical synthesis strategies, the pathways of mechanochemical abrasion, thermal shockwave and laser irradiation can serve as versatile approaches to synthesize SACs[36–39]. But customized settings or specific equipment can be required for applying these approaches[36]. Therefore, a straightforward and cost-effective universal synthesis approach for scale production of SACs is desired but remains challenging[1,10,11].

[1]School of Chemical Engineering and Advanced Materials, The University of Adelaide, Adelaide, South Australia, Australia. [2]Christchurch Regenerative Medicine and Tissue Engineering (CReaTE) Group, Department of Orthopedic Surgery & Musculoskeletal Medicine, Centre for Bioengineering & Nanomedicine, University of Otago, Christchurch, New Zealand. [3]Department of Bone and Joint, The First Affiliated Hospital of Dalian Medical University, Dalian, China. [4]Australian Synchrotron, ANSTO, Clayton, Victoria, Australia. [5]Beijing National Laboratory for Condensed Matter Physics, Institute of Physics, Chinese Academy of Science, Beijing, China. [6]The First Affiliated Hospital of Zhengzhou University, Zhengzhou, China. [7]These authors contributed equally: Fangxi Xie, Xiaolin Cui, Xing Zhi. e-mail: s.qiao@adelaide.edu.au

Recently, three-dimensional (3D) printing techniques have been developed as unique manufacturing routes for mass production of targeted products. The use of 3D-printing has been considered a simple approach as it can directly fabricate target materials and avoid complex wet-chemistry processes[40,41]. In contrast to conventional subtractive manufacturing process, 3D-printing techniques work more economically by effectively eliminating the generation of waste materials during the manufacturing process[40–42]. Introduction of cheaper 3D-printing machines and an increasing number of commercially available printable materials offer easily accessible opportunities to substantially reduce the overall cost of final products[40–44]. Additionally, 3D-printing can automatically and efficiently construct materials with customized geometric designs from millimetres to beyond metre scale, paving a pathway for industrial-scale production[44–47]. However, despite the popularity of 3D-printing techniques, mainly in the biomedical field, its application in SAC production remains elusive.

Herein, we report a universal 3D-printing synthesis approach to directly construct a library of SACs. By mixing the printing ink with transition metal precursors, a straightforward 3D-printing approach was developed to synthesize various SACs. Minimal alteration of the atomic dispersion was seen with synthetic variations on centre atoms, loadings of the centre atoms, coordination environments and spatial geometries, demonstrating the universality of this approach. The employment of natural polymers, including gelatin and gelatin methacryloyl (GelMA), as printing ink offers an accessible and affordable route[32,33]. Furthermore, the automatic and direct fabrication of centimetre-size SAC precursors avoids complicated wet-chemistry processes. These two merits of reduced costs and added convenience identify its great potential for mass production of SACs. In addition, as a proof-of-concept, the performance of 3D-printed SACs was evaluated by a nitrate reduction reaction, showcasing their potential application as electrocatalysts.

Results and discussion

Synthesis and structural characterization of Fe3DSAC

As shown in Fig. 1a, several steps are involved in the 3D-printing approach. Initially, the hydrogel containing gelatin and GelMA was mixed with the corresponding transition metal precursors to formulate the printing ink. The 3D structure was directly and automatically constructed by the 3D-printing technique (a typical printing process is shown in the Supplementary Video 1). Afterwards, the as-printed sample was freeze-dried to remove residual water. Then, the 3D-printed SACs were achieved through the pyrolysis process of as-dried samples to anchor metal single atoms onto the gelatin/GelMA-derived carbon. To further elucidate the fabrication process, we take the synthesis of Fe 3D-printed SAC with a precursor hole size of 1.0 mm (denoted as Fe3D-SAC or Fe3DSAC 1.0 mm) as an example. In this process, $Fe(acac)_3$ was employed as the Fe single-atom precursor. As shown in Fig. 1b, the 3D centimetre-size precursor was constructed via 3D-printing technique. Typical scanning electron microscopy (SEM) and the corresponding energy dispersive X-ray (EDX) images of the typical as-pyrolysis product with hole size of 2.0 mm, shown in Fig. 1c and Supplementary Fig. 1, prove that the pristine structure from the 3D-printing technique was maintained after the pyrolysis process. The related thermogravimetric analysis result (Supplementary Fig. 2) shows that most of the mass loss happened between 300 and 400 °C. Additionally, EDX images indicate the homogenous distribution of carbon, nitrogen and iron in the as-prepared Fe3DSAC (ref. [26]). As a comparison, an analogue pure carbon sample was prepared with the same procedure without the presence of $Fe(acac)_3$ and named as 3DCarbon. The X-ray diffraction (XRD) results of Fe3DSAC and 3DCarbon (Supplementary Fig. 3) validate the amorphous nature of carbon substrates and the absence of iron nanoparticles in the as-prepared Fe3DSAC. According to the high-resolution high-angle annular dark-field scanning transmission electron microscope (HAADF-STEM; Fig. 1d and Supplementary Fig. 4) image, iron single atoms are clearly observed as the dots labelled with white circles, demonstrating the atomic isolation of iron sites[48]. Furthermore, in the extended X-ray absorption fine structure (EXAFS) results shown in Fig. 1e, different from the strong wavelet transform (WT) signal (focused at $k = 8.3$ Å, $r = 2.2$ Å) of bulk Fe metal (denoted as Fe metal ref in Fig. 1e,f), the WT signal of Fe3DSAC is focused at $k = 6.0$ Å, $r = 1.5$ Å, indicating an absence of Fe–Fe bonds in the Fe3DSAC sample. The similarity between WT-EXAFS plots of Fe3DSAC and $Fe(acac)_3$ verifies the dispersed atom nature of iron sites in Fe3DSAC (refs. [49,50]). Alternatively, as shown in the Fourier-transform (FT) EXAFS spectrum of the bulk Fe metal (Fig. 1f), the Fe–Fe coordination path between 2.0 and 2.5 Å (shaded light red) is absent in the FT-EXAFS spectrum of Fe3DSAC. We conclude that the FT-EXAFS analysis confirms the atomic dispersion of iron atoms in Fe3DSAC. The notable difference in the spectra of X-ray absorption near edge structure (XANES) of the bulk Fe metal and Fe3DSAC, shown in Supplementary Fig. 5, also indicates a notable difference in coordination environments between the materials[29]. Additionally, the FT-EXAFS curve of Fe3DSAC exhibits more similarity to $Fe(acac)_3$ and Fe_2O_3 than iron foil, verifying the absence of iron clusters and iron nanoparticles in the Fe3DSAC sample. With regards to its coordination environment, the Fe L-edge and O K-edge results (Supplementary Fig. 6) suggest that the coordination environment of Fe3DSAC is more closely linked to the one for $Fe(acac)_3$ as opposed to that of FePc. This indicates that the bonding between Fe and the carbon-based substrate could be Fe–O.

Furthermore, the local coordination configuration of Fe3DSAC was further investigated by quantitative least-squares EXAFS curve-fitting analyses. Specifically, the major peak of $Fe(acac)_3$ locates at 1.52 Å while the one of Fe3DSAC shifts to 1.76 Å, indicating some alterations occur at the coordination environment of Fe3DSAC. FT-EXAFS fitting results suggest the shift of Fe–X peaks (shaded by light blue in Fig. 1f) due to the introduction of chloride in the post-treatment process. As shown in Fig. 1g, Supplementary Fig. 7 and Supplementary Table 2, the best-fit results for Fe3DSAC consist of two backscattering paths: Fe–O and Fe–Cl. The coordination numbers of oxygen and chloride are estimated to be 4 and 1, respectively. Additionally, the X-ray photoelectron spectroscopy (XPS) results also confirm the existence of Fe–O and Fe–Cl bonds for Fe3DSAC (Supplementary Fig. 8). Taken together, the fitting results confirm a $Fe–O_4–Cl$ moiety for the Fe3DSAC sample. This proposed coordination configuration of $Fe–O_4–Cl$ is illustrated by the scheme shown in the inset of Fig. 1g.

Universality on central elements

We extended the synthesis approach to other representative transition metals to confirm the universality of central atoms of this approach. By simply replacing $Fe(acac)_3$ with other metal acetylacetonates, for example, $Co(acac)_2$, $Ni(acac)_2$, $Cu(acac)_2$, $Zn(acac)_2$ and $Pt(acac)_2$, many SACs (denoted as CoSAC, NiSAC, CuSAC, ZnSAC and PtSAC, respectively) were obtained using similar procedures. In the HAADF-STEM image of PtSAC (Fig. 2a), the atomically dispersed nature of Pt single-atom sites can be confirmed. Furthermore, the homogenous dispersion of platinum, nitrogen and carbon in the transmission electron microscopy (TEM) EDX elemental mapping results (Supplementary Fig. 9) confirm the absences of obvious platinum metallic particles in PtSAC. In the corresponding WT-EXAFS contour plots (Fig. 2b), the absence of WT-EXAFS signal at $r > 2.0$ Å indicates the atomic dispersion nature of platinum sites in the as-prepared SACs[49,50]. The absence of Pt clusters and nanoparticles in the PtSAC is also supported by the absence of the Pt–Pt path between 2.5 and 3.0 Å in the FT-EXAFS (Supplementary Fig. 10a) and the notable differences in XANES spectra (Supplementary Fig. 10b) between PtSAC and the platinum metallic reference (denoted as Pt metal ref). The absence of metal–metal paths between 2.0 and 2.5 Å (FT-EXAFS) as shown in Fig. 2c and Supplementary Fig. 11 for CuSAC, NiSAC, CoSAC and ZnSAC indicates the successful preparation of SACs of corresponding transition metals. Additionally, the fitting results confirm the $M–O_4$ moieties for these SAC samples (Supplementary Fig. 12).

https://doi.org/10.1038/s44160-022-00193-3

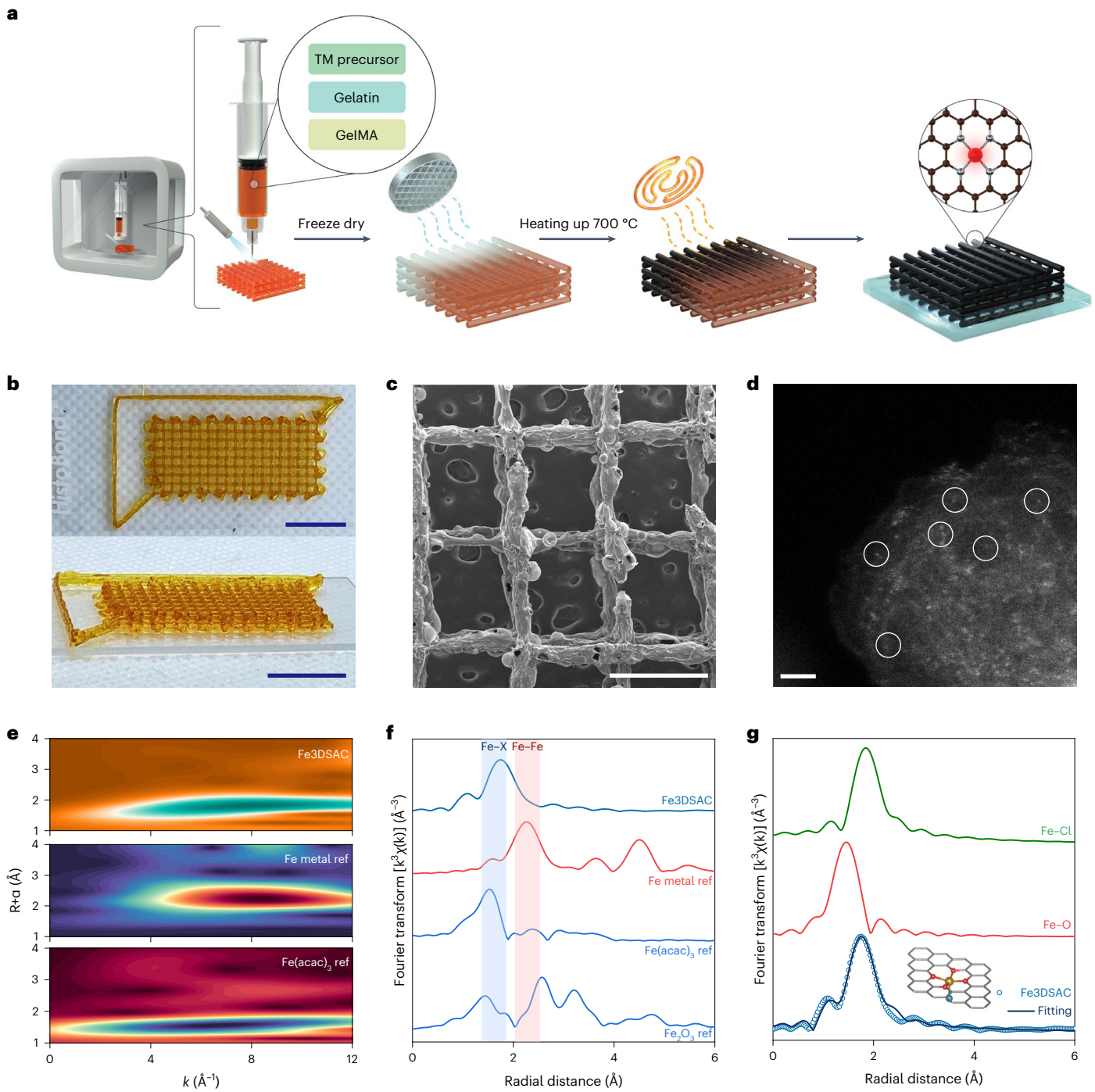

Fig. 1 | The synthesis procedure. a, Synthesis procedure for 3D-printed SACs. **b**, Digital photographs of the as-prepared precursor. Scale bar, 1 cm. **c**, SEM image of Fe3DSAC with the precursor hole size of 2.0 mm. Scale bar, 1 mm. **d**, HAADF-STEM image of isolated iron sites (circled in white). Scale bar, 2 nm. **e**, WT-EXAFS contour plots for the Fe3DSAC and reference samples. **f**,**g**, Normalized FT-EXAFS spectra (**f**) and Fe K-edge EXAFS fitting analyses (**g**) for Fe3DSAC in R Space. The blue coloured strip in (**f**) indicates the bonds between iron atom and non-metal elements; the red coloured strip indicates the Fe–Fe bonds. The inset in (**g**) shows the structure of a Fe–O_4–Cl local coordination derived from the EXAFS result, where the gold, red and cyan-coloured spheres represent Fe, O and Cl atoms, respectively.

Furthermore, the homogenous dispersion of metal, nitrogen and carbon in the atomic-resolution HAADF-STEM images (Supplementary Figs. 13 and 14) and TEM EDX elemental mapping results (Supplementary Figs. 15–18) confirm the absences of obvious metallic particles in as-prepared SACs. Additionally, as shown in Supplementary Fig. 19, the absences of any crystalline peak in the XRD patterns of as-prepared samples offer further evidence for the successful preparation of SACs. Furthermore, as shown in Supplementary Figs. 20–23, this approach can also be extended toward synthesizing IrSAC and MnSAC. Therefore, the synthesis approach developed from this study is universal to prepare SACs with different transition metals as centre atoms.

To confirm the universality of this approach, we further adapted the synthesis approach to other common parameters, for example, metal loadings, coordination environments and spatial geometries.

https://doi.org/10.1038/s44160-022-00193-3

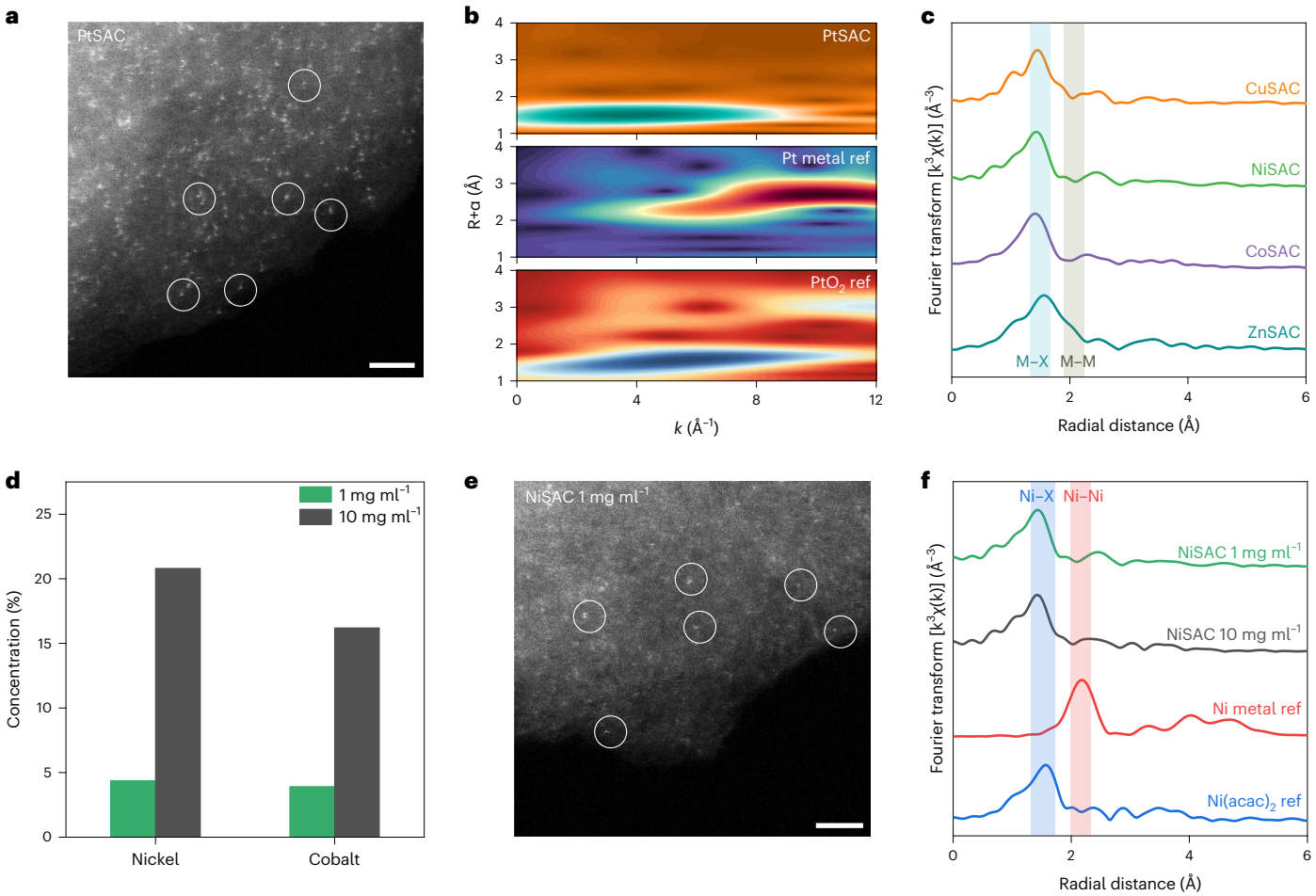

Fig. 2 | Universality of elements and metal loadings. a, Atomic-resolution HAADF-STEM image of isolated platinum sites (circled in white). Scale bar, 2 nm. **b**, WT-EXAFS contour plots for the PtSAC and reference samples (FT-EXAFS spectrum PtSAC, see Supplementary Fig. 10). **c**, Normalized FT-EXAFS spectra of CuSAC, NiSAC, CoSAC and ZnSAC. The aqua coloured strip in (**c**) indicates the bonds between metal elements and non-metal elements (marked as M–X in the figure); the tan coloured strip indicates the metal–metal bonds (marked as M–M in the figure). **d**, Metal loadings achieved in corresponding Co and Ni samples. **e**, Atomic-resolution HAADF-STEM image of NiSAC 1 mg ml^{-1}. Scale bar, 2 nm. **f**, Normalized FT-EXAFS spectra of Ni samples with different metal loadings and reference samples. The blue coloured strip in (**f**) indicates the bonds between nickel atom and non-metal elements; the red coloured strip indicates the nickel–nickel bonds.

Universality on metal loadings

Different concentrations of corresponding metal (Co and Ni) acetylacetonates in the printing ink (1 and 10 mg ml^{-1}) were applied to evaluate its universality on metal loadings. Inductively coupled plasma results (Fig. 2d) reveal the loadings of Ni-related samples with various $Ni(acac)_2$ concentrations (denoted as NiSAC 1 mg ml^{-1} or NiSAC above and NiSAC 10 mg ml^{-1}) are 4.3% and 20.8%, respectively. The loadings of corresponding CoSACs (denoted as CoSAC 1 mg ml^{-1} or CoSAC above and CoSAC 10 mg ml^{-1}) were 3.9% and 16.2%, respectively. In the corresponding HAADF-STEM image (Fig. 2e), as indicated by white cycles, the atomic dispersion nature of nickel atoms can be confirmed. Furthermore, the absence of the Ni–Ni path between 2.0 and 2.5 Å in FT-EXAFS (Fig. 2f and Supplementary Fig. 24a) and the absence of WT-EXAFS signal at $r > 2.0$ Å in WT-EXAFS (Supplementary Fig. 25) demonstrate the atomic dispersion nature of Ni atoms in the corresponding samples. A similar conclusion can be drawn for the Co samples based on the corresponding FT-EXAFS and WT-EXAFS results (Supplementary Figs. 26 and 24b). Additionally, as shown in Supplementary Fig. 27, the comparable XANES curves of samples with different loadings indicate that the impact of various metal loadings on the coordination environments is negligible. To further demonstrate the capability of regulating transition metal loadings, we employed various printing inks with different concentrations of $Fe(acac)_3$ to synthesize FeSACs with different loadings. The EXAFS characterizations (Supplementary Fig. 28) verify the dispersed atomic nature of iron sites in the as-prepared samples with different concentrations. The inductively coupled plasma results suggest that the iron contents in the corresponding samples are 7.0% and 12.1%, respectively. Combined with the results of Co and Ni samples, the capability to regulate the metal loadings is demonstrated.

Universality on coordination environments

As one of the most important features of SACs is their tunable coordination environments, various approaches have been applied to change coordination environments of as-prepared SACs in this study. First, different transition metal (Zn and Cu) phthalocyanine (ZnPc and CuPc) salts were applied to further verify the alteration on coordination environments due to the adjustment of transition metal precursors. HAADF-STEM images, shown in Fig. 3a,b, demonstrate the atomic dispersion nature of zinc atoms in the as-prepared samples (the one with ZnPc is denoted as ZnSAC PC while the one with $Zn(acac)_2$ is denoted as ZnSAC AC or ZnSAC above) derived from different zinc precursors. Furthermore, as shown in Supplementary Fig. 29, the absences of the Zn–Zn path between 2.0 and 2.5 Å and WT-EXAFS signal at $r > 2.0$ Å indicates mono-atomic dispersion of Zn atoms in the corresponding samples.

https://doi.org/10.1038/s44160-022-00193-3

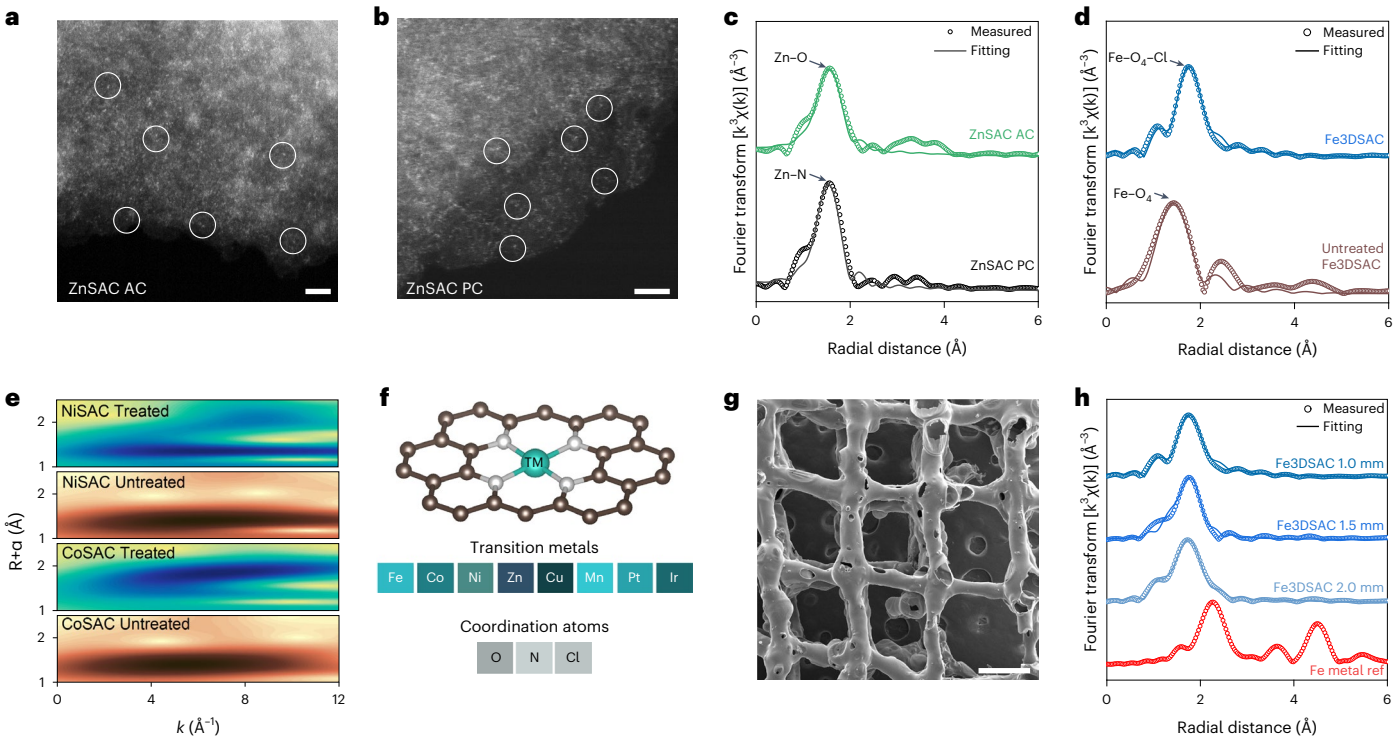

Fig. 3 | Universality of coordination environments and spatial geometries. **a**,**b**, Atomic-resolution HAADF-STEM images of ZnSAC AC (**a**) and ZnSAC PC (**b**). Scale bar, 2 nm. **c**, Zn K-edge EXAFS fitting analyses for as-prepared Zn samples in R Space. **d**, Fe K-edge EXAFS fitting analyses for Fe3DSAC and the untreated Fe3DSAC sample in R Space. **e**, WT-EXAFS contour plots for the treated and untreated samples (NiSACs and CoSACs). **f**, Scheme showing the capability of tuning central atoms and coordination environments of this approach. **g**, SEM image of Fe3DSAC with the precursor hole size of 1.5 mm. Scale bar, 0.5 mm. **h**, Normalized FT-EXAFS spectra and fitting results of Fe samples from different geometries and reference sample.

A similar conclusion can be reached for the Cu samples based on the corresponding FT-EXAFS and WT-EXAFS results (Supplementary Fig. 30). These results demonstrate the capability of applying different precursors to prepare SACs by this approach.

Additionally, as shown in Fig. 3c and Supplementary Table 2, the FT-EXAFS curve of ZnSAC AC shows up with a major peak located at 1.57 Å. As a comparison, the main peak of ZnSAC PC locates at 1.53 Å. This difference on peak locations can be attributed to the difference between Zn–O bonds and Zn–N bonds. Furthermore, the best FT-EXAFS fitting results of ZnSAC AC suggest that it consists of one major backscattering path: Zn–O, while the coordination number of oxygen is estimated to be 4. Therefore, these results confirm a Zn–O_4 moiety for ZnSAC AC. As regards ZnSAC PC, the fitting results suggest it consists of Zn–N coordination configuration with a coordination number of 4, indicating a Zn–N_4 moiety. Consequently, the capability of employing different precursors might bring the capability to modify the coordination environments[51–53].

To further evaluate the universality of our approach, several widely used natural polymers in 3D-printing were employed to synthesize the SACs containing iron. In the EXAFS results (Supplementary Fig. 31) of as-prepared samples, the Fe–Fe coordination path between 2.0 and 2.5 Å (shaded light red) is absent, verifying the absence of iron clusters and iron nanoparticles in the as-prepared samples derived from these natural polymers as scaffold basements.

In addition to modification of precursors, post-treatment could be another effective approach to directly alter the coordination environments[54]. Soaking in hydrochloride acid was selected as a typical post-treatment process to evaluate the capability to modify coordination environments through post-treatment process. Specifically, as shown in the FT-EXAFS results (Fig. 3d and Supplementary Table 2), the main bonding peak of untreated Fe3DSAC sample locates at 1.45 Å. Furthermore, the FT-EXAFS fitting results indicate that the untreated sample has a moiety of Fe–O_4. As opposed to that of the untreated sample, as shown in Fig. 1g and 3d, the main FT-EXAFS peak of treated Fe3DSAC shifted to 1.76 Å, compared with the main bonding peak of untreated Fe3DSAC sample located at 1.45 Å. This demonstrates that the treated Fe3DSAC possesses a moiety of Fe–O_4–Cl. The successful alteration of Fe–O_4 moiety to Fe–O_4–Cl moiety validates that the post-treatment approach to change coordination environments remains effective in 3D-printed SACs[54–56]. To further evaluate the universality of post-treatments on modifications of as-prepared samples, samples with different central transition metal atoms (Co, Ni, Mn) were prepared following a similar post-treatment process stated above. As shown in Supplementary Fig. 32, all as-prepared samples exhibit broader peaks located between 1.5 and 2.0 Å. Considering that the corresponding metal–metal paths of these three elements locate at above 2.0 Å, the FT-EXAFS results demonstrate the absence of metal nanoparticles and clusters in these samples. Furthermore, as shown in Fig. 2c, the main peaks of untreated samples are located between 1.4 Å and 1.5 Å. A peak closed to 2.0 Å shows up in each treated sample, which can be attributed to the metal–chloride bonds[54–56]. As shown in Fig. 3e, the additional WT signals focused at around $k = 8.0$ Å, $r = 2.0$ Å also reveal the existences of metal–chloride bonds in treated NiSAC and treated CoSAC. The above results of changing the coordination environments of iron, nickel and cobalt single-atom sites suggest that the coordination configurations of 3D-printed samples can be easily tuned through changing the precursor or employing post-treatment procedure, demonstrating the highly universal nature of our approach. As suggested by the results, gelatin/GelMA can be employed to prepare a library of SACs with various central-atom and different coordination environments, as shown in the scheme (Fig. 3f).

https://doi.org/10.1038/s44160-022-00193-3

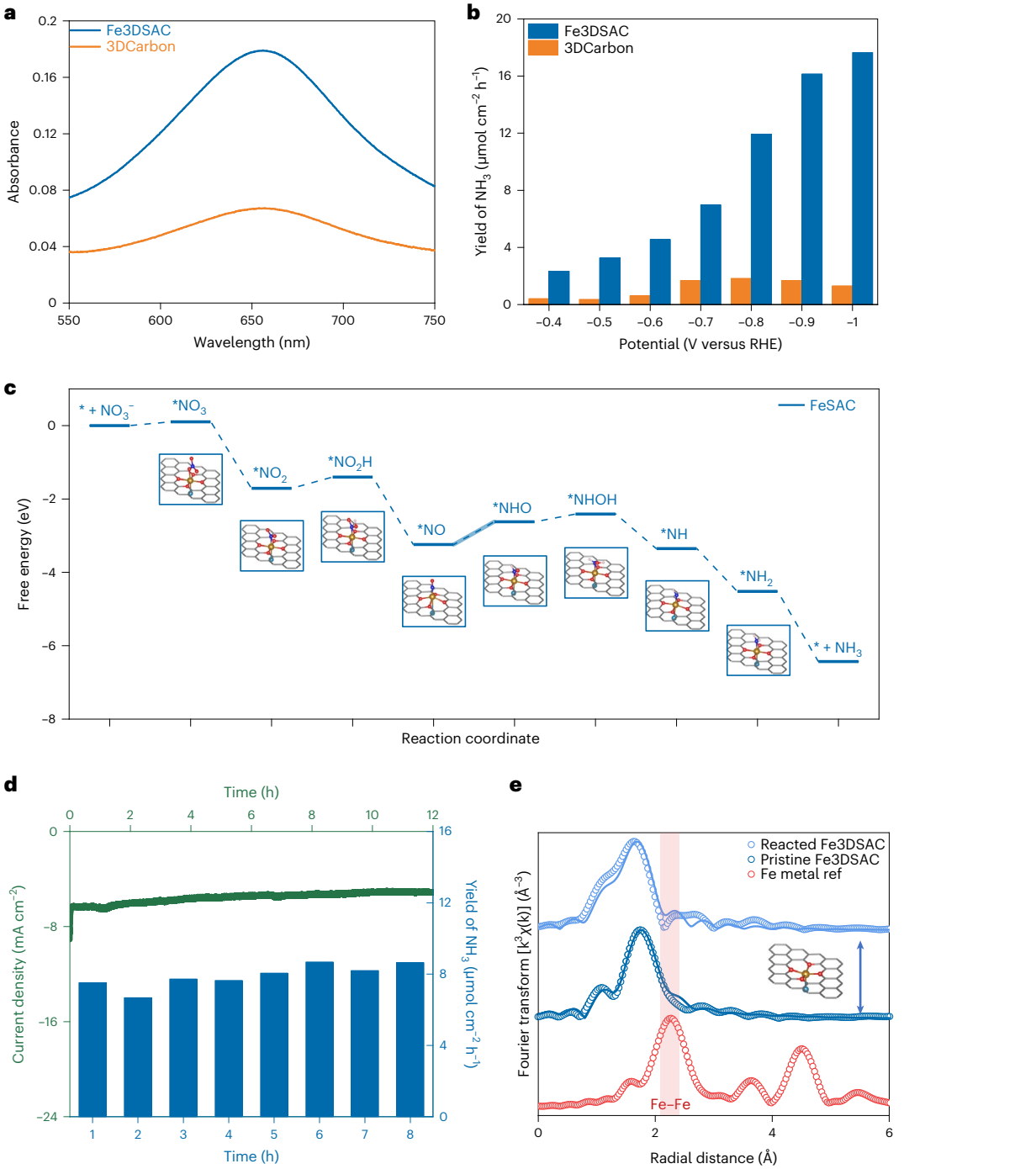

Fig. 4 | Electrocatalytic performance of 3D-printed SACs for nitrate reduction reaction. a, Comparison between the NH_3 yield of Fe3DSAC and 3DCarbon at −0.6 V versus RHE. **b**, NH_3 yield at varying potentials in 0.10 M KOH with addition of 10 mM NO_3^-. **c**, Free energy diagram showing the minimum energy pathway of iron single-atom site (enlarged optimized configurations can be found in Supplementary Table 1). **d**, Stability tests for Fe3DSAC at −0.5 V versus RHE in 0.10 M KOH with 0.10 M NO_3^-. **e**, Ex situ normalized FT-EXAFS spectra and fitting results of reacted Fe3DSAC, pristine Fe3DSAC and Fe metal reference. The insets in (**c**,**e**) show (**c**) optimized configurations of reaction intermediates and (**e**) the structure of a Fe−O_4−Cl local coordination derived from the EXAFS result. Colour code: gold, iron; red, oxygen; cyan, chlorine; blue, nitrogen; white, hydrogen; grey, carbon.

Universality on spatial geometries

One advantage to the 3D-printing approach is the capability to tune the geometries. As shown in Supplementary Fig. 33, the hole sizes of precursors were rationally customized between 1.0 mm, 1.5 mm and 2.0 mm. As shown in Figs. 1c, 3g and Supplementary Fig. 34, the 3D-printed structures remained after the calcination, demonstrating the capability to maintain the microstructure from the 3D-printing technique even after the high-temperature processing. Additionally, as shown in Supplementary Fig. 35, different patterns of 3D-printed electrode can also be achieved by changing the printing parameters, showcasing the capability to tune the spatial geometry of SACs. In addition, as shown in Supplementary Fig. 36, the size of the printing precursor was expanded to 4 × 2 cm. It is expected the size could be further increased using a commercial-scale 3D-printer. Taken together, the 3D-printing technique offers another unique capability to infinitely extend the size of the as-prepared sample. Afterwards, the atomic dispersion nature

of iron sites in 3D-printed SACs were demonstrated by FT-EXAFS (Fig. 3h) and WT-EXAFS (Supplementary Fig. 37) analysis. The fitting results suggest a moiety of Fe–O_4–Cl for all the as-prepared samples. It demonstrates that different settings on 3D-printing make ignorable alterations on the single-atom dispersion nature and coordination environments to the 3D-printed samples.

Performance evaluation of 3D-printed SACs

As a proof-of-concept, to evaluate the potential of the as-obtained SACs, Fe3DSAC was employed as an electrocatalyst for nitrate reduction reaction (eNO_xRR) as iron single-atom exhibited superior performance in such a reaction[48,57,58]. The eNO_xRR performance of Fe3DSAC was evaluated in an Ar-saturated 0.10 M KOH aqueous solution with 10 mM NO_3^-. The detailed electrochemical cell configuration is shown in Supplementary Fig. 38. The as-prepared Fe3DSAC exhibited a notably increased ammonia production, compared with 3DCarbon. Specifically, as quantified by UV-Vis measurements (Fig. 4a and Supplementary Fig. 39), the yield of ammonia of Fe3DSAC at −0.6 V versus reversible hydrogen electrode (RHE) was ~4.55 μmol cm^{-2} h^{-1} which was about 7.5 times the 0.61 μmol cm^{-2} h^{-1} from 3DCarbon. Furthermore, as shown in Fig. 4b and Supplementary Figs. 40 and 41, Fe3DSAC exhibited higher yields of ammonia than 3DCarbon at all the potentials, indicating good function of the 3D-printed SACs. Additionally, the electrocatalytic performance can be further tuned by changing the central elements and spatial geometries of 3D-printed SACs (Supplementary Fig. 42). Based on the previous fitting results of FT-EXAFS, we constructed models of iron single-atom site (denoted as FeSAC) with a moiety of Fe–O_4–Cl to discuss the underlying mechanism of as-prepared single-iron-atom catalyst. The density functional theory (DFT) calculations, shown in Fig. 4c and Supplementary Fig. 43, reveal that the most likely path is the one with the protonation of *NO to *NHO, followed by the formation of *NHOH and *NH key reaction intermediates. It also suggests that, among all the elementary steps, the potential limiting step on FeSAC is the protonation of *NO to *NHO/*NOH, at which the formation of *NHO exhibited more favourable thermodynamics. Eventually, electrocatalytic stability was evaluated by replacing the electrolytes every hour for eight cycles. As shown in Fig. 4d, no meaningful change to ammonia production and negligible variation in the current density was observed during long-term electrolysis, further demonstrating the stability of as-prepared Fe3DSAC. The ex situ XANES results and the fitting results of FT-EXAFS test (Fig. 4e, Supplementary Fig. 44 and Supplementary Table 2) confirm that the Fe–O_4–Cl moiety of Fe3DSAC was maintained after eNO_xRR, indicating the stability of single-atom sites in such a 3D-printing structure.

Conclusions

Taken together, compared with previous reported general synthesis approaches for SACs, the 3D-printing approach with GelMA and gelatin described herein to produce SACs is straightforward, affordable and effective for mass production. A highly universal synthesis approach was developed to fabricate different SACs using various synthesis parameters, including centre elements, metal loadings of centre elements, coordination environments and spatial geometries, with minimal alteration of the atomic dispersion. Furthermore, the 3D-printed SAC exhibited solid performance as an electrocatalyst for nitrate reduction reaction, showcasing the potential of 3D-printed SACs for downstream catalytic applications. More importantly, the 3D-printing technique not only offers capability to obtain SACs with desired geometry for different reactions but also provides a promising avenue to scale manufacture SACs, paving the way for implementing SACs to achieve sustainable production of valuable fuels and chemicals.

Methods

Synthesis of GelMA

The synthesis of GelMA was based on the previous study[59]. Briefly, 45 g gelatin was dissolved in 450 ml phosphate-buffered saline at 50 °C with vigorous stirring. After the full dissolution of gelation, an additional 27 g methacrylic anhydride was added based on the total mass of gelation (0.6 g methacrylic anhydride per 1.0 g gelatin). The reaction was carried out at 50 °C for 1 h, followed by dialysis of the solution against MilliQ water for 5 days with changing water twice per day, to remove the unreacted monomers. After the dialysis, the solution was sterilely lyophilized to store at −20 °C for future use.

Synthesis of Fe3DSAC and 3DCarbon

GelMA (0.4 g) and gelatin (0.2 g) were dissolved in 3.6 ml water to form the base printing ink with 10 wt% GelMA and 5 wt% gelatin. $Fe(acac)_3$ aqueous suspension (0.4 ml of 100 mg ml^{-1}) was mixed together with the base printing ink to formulate the desired printing ink (~10 mg ml^{-1} $Fe(acac)_3$) using a water sonication bath at 45 °C. Before printing, 0.1 ml of 1 mM tris(2,2-bipyridyl) dichlororuthenium (II) hexahydrate and 0.1 ml of 10 mM sodium persulfate were added as photo initiators. The printing ink of 3DCarbon was prepared following the same procedure without the addition of the $Fe(acac)_3$.

Three-dimensional-printed Fe3DSAC or 3DCarbon construction was fabricated using a BioScaffolder (SYS+ENG, Germany) 3D printer. The printing head temperature was 27 °C and the temperature for base plate was 4 °C. The specific printing parameters were: inner diameter of the printing head was 300 μm, XY-plane speed of 550 mm min^{-1}, Z-speed of 800 mm min^{-1}, auger speed of 3.5 rpm and fibre spacing of 1, 1.5 or 2 mm in a 0–90° repeating pattern. After eight layers were 3D printed, the printed samples were cross-linked under visible light with an intensity at 30 mW cm^{-2} for 3 min, followed by lyophilization.

Afterwards, the as-prepared precursor was placed in a tube furnace and then heated to 700 °C for 2 h at a heating rate of 2 °C min^{-1} under argon atmosphere followed by natural cooling to room temperature. The as-prepared products were collected for further use or treatment.

Synthesis of CoSAC, NiSAC, ZnSAC, CuSAC, IrSAC, MnSAC and PtSAC

The synthesis procedure was similar to that of Fe3DSAC but replacing the $Fe(acac)_3$ by corresponding metal acetylacetonates ($Co(acac)_2$, $Ni(acac)_2$, $Zn(acac)_2$, $Cu(acac)_2$, $Ir(acac)_3$, $Mn(acac)_3$ and $Pt(acac)_2$). The detailed print ink preparation process is described as follows: the base printing ink was prepared following the same procedure as above. Specifically, 0.4 ml of aqueous suspension (10 mg ml^{-1}) of corresponding metal acetylacetonates were mixed together with the base printing ink to formulate the desired printing ink (~1 mg ml^{-1}) using a water sonication bath at 45 °C. The subsequent preparation processes were similar to those for Fe3DSAC but without the post-treatment.

Synthesis of NiSAC 1 mg ml^{-1}, NiSAC 10 mg ml^{-1}, CoSAC 1 mg ml^{-1} and CoSAC 10 mg ml^{-1}

The synthesis procedure was similar to that for the single-atom analogue but with increased concentration of corresponding metal acetylacetonates from 1 mg ml^{-1} to 10 mg ml^{-1}. The detailed print ink preparation process is described as follows: the base printing ink was prepared following the same procedure as above. Specifically, 0.4 ml of aqueous suspension (10 mg ml^{-1}) of corresponding metal (Ni and Co) acetylacetonates were mixed together with the base printing ink to formulate the desired printing ink (~1 mg ml^{-1}) using a water sonication bath at 45 °C for NiSAC 1 mg ml^{-1} and CoSAC 1 mg ml^{-1}. Additionally, due to the limited solubility of metal acetylacetonates in water, 50 mg of corresponding metal (Ni and Co) acetylacetonates were dissolved in 0.5 ml ethanol to prepare the corresponding suspension (100 mg ml^{-1}). The as-prepared ethanol solution of corresponding metal acetylacetonates (0.4 ml) was mixed with the base printing ink to formulate the desired printing ink (~10 mg ml^{-1}) using a water sonication bath at 45 °C for NiSAC 10 mg ml^{-1} and CoSAC 10 mg ml^{-1}. The subsequent preparation processes were similar to those for Fe3DSAC but without the post-treatment.

Synthesis of ZnSAC AC, ZnSAC PC, CuSAC AC and CuSAC PC

The synthesis procedure was similar to those of the single-atom analogues but with replacement of metal acetylacetonates ($Cu(acac)_2$, $Zn(acac)_2$) by corresponding metal phthalocyanines (copper phthalocyanine, zinc phthalocyanine). The detailed print ink preparation process is described as follows: the base printing ink was prepared following the same procedure above. Specifically, 0.4 ml of aqueous suspension (10 mg ml^{-1}) of corresponding metal (Zn and Cu) acetylacetonates were mixed together with the base printing ink to formulate the desired printing ink (~1 mg ml^{-1}) using a water sonication bath at 45 °C for ZnSAC AC and CuSAC AC. Additionally, 0.4 ml of aqueous suspension (10 mg ml^{-1}) of corresponding metal (Zn and Cu) phthalocyanines was mixed together with the base printing ink to formulate the desired printing ink using a water sonication bath at 45 °C for ZnSAC PC and CuSAC PC. The subsequent preparation processes were similar to those of Fe3DSAC but without the post-treatment.

Synthesis of FeSAC by other polymers

For gelatin, 0.75 g gelatin was dissolved in 5.0 ml water to form the base printing ink with 15 wt% gelatin. $Fe(acac)_3$ aqueous suspension (0.5 ml of 10 mg ml^{-1}) was mixed together with the base printing ink to formulate the desired printing ink (~1 mg ml^{-1} $Fe(acac)_3$) using a water sonication bath at 45 °C. Additionally, 0.1 ml of 1 mM tris(2,2-bipyridyl) dichlororuthenium (II) hexahydrate and 0.1 ml of 10 mM sodium persulfate were added as photo initiators. The subsequent preparation processes were similar to those for Fe3DSAC but without the post-treatment.

For agarose, 50 mg agarose was dissolved in 5.0 ml water using a water bath at 75 °C. $Fe(acac)_3$ aqueous suspension (0.5 ml of 10 mg ml^{-1}) was mixed together with the base printing ink to formulate the desired printing ink (~1 mg ml^{-1} $Fe(acac)_3$) using a water sonication bath at 75 °C. With the cool down to room temperature, the hydrogel was achieved, followed by lyophilization. The subsequent preparation processes were similar to those of Fe3DSAC but without the post-treatment.

For alginate, 5.2 ml of 1 wt% sodium alginate aqueous solution was mixed with 0.5 ml of $Fe(acac)_3$ aqueous suspension (10 mg ml^{-1}). Afterwards, 3.6 ml of 0.2 M $CaCl_2$ aqueous solution was poured into the mixed solution of sodium alginate and $Fe(acac)_3$ to formulate the desired printing ink, followed by lyophilization. The subsequent preparation processes are similar to those for Fe3DSAC but without the post-treatment.

Post-treatment process for chloride coordination

After the calcination, the as-prepared products were directly soaked in 1.0 M hydrochloric acid at 60 °C for 18 h. Following washing with distilled water three times, the treated samples were placed in an oven at 60 °C overnight to dry. Specifically, it is worth noting that all Fe3DSAC samples went through this post-treatment process expect for the untreated one.

Materials characterization

The morphology of the samples was characterized using FEI Quanta 450 SEM operated at 20.0 kV and FEI Titan Themis 80-200 TEM operated at 200.0 kV. The absorbance data of spectrophotometer were collected on a SHIMADZU UV-2600 UV-Vis spectrophotometer. XRD patterns were obtained using a Bruker D8 ADVANCE ECO X-ray diffractometer with Cu Kα radiation.

X-ray absorption spectra were collected on the X-ray Absorption Spectroscopy and Soft X-ray Spectroscopy beamline at Australian Synchrotron. All the as-prepared SACs were granulated and measured at room temperature in fluorescence excitation mode. The corresponding reference samples were mixed with cellulose and measured in a transmission mode using standard He-filled chambers. The EXAFS raw data were background-subtracted, normalized and FT by standard procedures using ATHENA module implemented in the IFEFEIT software packages[60]. Least-squares curves fitting analyses of the EXAFS $\chi(k)$ data was carried out using the ARTEMIS program[60]. The WT of EXAFS raw data were conducted by a suite of software modules developed by Marina Chukalina (IMT-RAS) and Harald Funke (IRC-FZR)[49,50].

For the metal loadings test, each Fe, Co and Ni sample was placed in a 50-ml autoclave with a mixed solution of 7.5 ml distilled water and 2.5 ml of nitric acid (70%). After sealing, the autoclave was kept at 150 °C for 8 h to dissolve the carbon. The obtained solutions were used to determine the contents of Fe, Co and Ni by an inductively coupled plasma mass-spectrometer (Agilent 8900x QQQ-ICP-MS).

Electrochemical measurements

Electrochemical data were collected with a CHI-760D electrochemical workstation (CHI Instrument, Inc.). An H-type cell with three-electrode system was used in the electrochemical measurement, in which a graphite-rod (φ6 mm × 65 mm) was used as counter electrode and an Ag/AgCl (filled with saturated KCl) as a reference electrode. The cathodic chamber was separated from the anodic chamber by an anion exchange membrane (Fumasep FAA-3-50). For 3D-printed samples, the as-prepared sample was fixed by a polytetrafluoroethylene (PTFE) replaceable electrode holder with platinum sheet as the conductive substrate and served directly as the working electrode. All experiments were carried out at room temperature and all potentials were referenced against RHE based on the Nernst equation ($E_{RHE} = E_{Ag/AgCl} + 0.0592 \times pH + 0.2$). The electrolyte used was 0.10 M KOH with various concentrations of nitrate/nitrite, which was purged with ultra-high purity Ar before the electrolysis process.

Quantification of NH_3 by the indophenol blue method[61]

Absorbance at 650 nm for each solution was collected with a UV-Vis spectrophotometer (SHIMADZU, UV-2600). A series of standard solutions with suitable NH_4Cl concentration diluted with 0.10 M KOH were prepared and tested to plot a calibration curve. The concentrations of ammonia in the test solutions were calculated directly from the calibration curve. Indophenol blue indicator was prepared by mixing three reagents. Chromogenic reagent (A): 5.0 g of sodium salicylate and 5.0 g of potassium sodium tartrate were dissolved in 100 ml of 1.0 M NaOH; oxidizing solution (B): 3.5 ml of sodium hypochlorite (available chlorine 10–15%) was added to 100 ml of deionized water; catalysing reagent (C): 0.2 g of sodium nitroferricyanide was dissolved in 20 ml of deionized water. For UV-Vis absorbance measurement, 2.0 ml of chromogenic reagent (A), 1.0 ml of oxidizing solution (B) and 0.2 ml of catalysing reagent (C) were added to the vial which contained 2.0 ml of the test solutions. After mixing and incubation for 1 h, the concentration of the produced indophenol blue was measured using UV-Vis absorbance spectrophotometer.

Computational details

All calculations were conducted using DFT with the Perdew–Burke–Ernzerhof (PBE) exchange-correlation functional in the VASP code[62–64]. The ionic cores were described by the projector-augmented wave method. A cut-off energy of 500 eV was used for plane wave expansion. During geometry optimization, the force convergence on each atom was set to be smaller than 0.02 eV $Å^{-1}$. A (4 × 4 × 1) Monkhorst-Pack k-point was applied to sample the Brillouin zone. The DFT-D3 method of Grimme was used in all calculations to address van der Waals interactions between atoms.

A one-layer 5 × 5 graphene supercell with 15 Å of vacuum space was used to build the FeSAC model. The computational hydrogen electrode model was employed for free energy calculations[65,66]. In this model, the free energy of an electron–proton pair at 0 V versus RHE is by definition equal to half of the free energy of gaseous hydrogen at 101,325 Pa. The free energies of intermediates were calculated by

$$G = E_{DFT} + ZPE - TS,$$

where E_{DFT}, ZPE, T and S were adsorption energy, zero point energy, temperature and entropy, respectively. The adsorption energy of $*NO_3$ was calculated with respect to solvated nitrate ions (NO_3^-) (ref. [67]). A 1.12 eV correction was applied to compensate for the DFT-calculated error of formation energies of HNO_3 (ref. [68]).

Data availability

All data supporting the findings of this study are available in the article and its Supplementary information. Source data are provided with this paper.

References

1. Ji, S. et al. Chemical synthesis of single atomic site catalysts. *Chem. Rev.* **120**, 11900–11955 (2020).
2. Qiao, B. et al. Single-atom catalysis of co oxidation using Pt_1/FeO_x. *Nat. Chem.* **3**, 634–641 (2011).
3. Wang, L. et al. Engineering single-atomic iron-catalyst-integrated 3D-printed bioscaffolds for osteosarcoma destruction with antibacterial and bone defect regeneration bioactivity. *Adv. Mater.* **33**, 2100150 (2021).
4. Chen, B., Zhong, X., Zhou, G., Zhao, N. & Cheng, H. M. Graphene-supported atomically dispersed metals as bifunctional catalysts for next-generation batteries based on conversion reactions. *Adv. Mater.* **33**, 2105812 (2021).
5. Wang, Y. et al. Advanced electrocatalysts with single-metal-atom active sites. *Chem. Rev.* **120**, 12217–12314 (2020).
6. Deng, Q. et al. Hydrogen-catalyzed acid transformation for the hydration of alkenes and epoxy alkanes over Co–N frustrated lewis pair surfaces. *J. Am. Chem. Soc.* **143**, 21294–21301 (2021).
7. Jung, E. et al. Atomic-level tuning of Co–N–C catalyst for high-performance electrochemical H_2O_2 production. *Nat. Mater.* **19**, 436–442 (2020).
8. Li, Y. et al. Synthesis of N-doped highly graphitic carbon urchin-like hollow structures loaded with single-Ni atoms towards efficient CO_2 electroreduction. *Angew. Chem. Int. Ed. Engl.* **61**, 202201491 (2022).
9. Zhang, H. B., Lu, X. F., Wu, Z. P. & Lou, X. W. Emerging multifunctional single-atom catalysts/nanozymes. *ACS Cent. Sci.* **6**, 1288–1301 (2020).
10. Wei, Y. S., Zhang, M., Zou, R. & Xu, Q. Metal–organic framework-based catalysts with single metal sites. *Chem. Rev.* **120**, 12089–12174 (2020).
11. Hai, X. et al. Scalable two-step annealing method for preparing ultra-high-density single-atom catalyst libraries. *Nat. Nanotechnol.* **17**, 174–181 (2022).
12. Xia, C. et al. General synthesis of single-atom catalysts with high metal loading using graphene quantum dots. *Nat. Chem.* **13**, 887–894 (2021).
13. Zhang, X. et al. A general method for transition metal single atoms anchored on honeycomb-like nitrogen-doped carbon nanosheets. *Adv. Mater.* **32**, 1906905 (2020).
14. Lai, W. H. et al. General π-electron-assisted strategy for Ir, Pt, Ru, Pd, Fe, Ni single-atom electrocatalysts with bifunctional active sites for highly efficient water splitting. *Angew. Chem. Int. Ed. Engl.* **58**, 11868–11873 (2019).
15. Zhao, L. et al. Cascade anchoring strategy for general mass production of high-loading single-atomic metal-nitrogen catalysts. *Nat. Commun.* **10**, 1278 (2019).
16. Zhao, Y. et al. Anchoring sites engineering in single-atom catalysts for highly efficient electrochemical energy conversion reactions. *Adv. Mater.* **33**, 2102801 (2021).
17. Jiao, L. et al. Chemical vapour deposition of Fe–N–C oxygen reduction catalysts with full utilization of dense Fe–N_4 sites. *Nat. Mater.* **20**, 1385–1391 (2021).
18. Liu, P. et al. Photochemical route for synthesizing atomically dispersed palladium catalysts. *Science* **352**, 797–800 (2016).
19. Zhang, H. et al. Isolated cobalt centers on $W_{18}O_{49}$ nanowires perform as a reaction switch for efficient CO_2 photoreduction. *J. Am. Chem. Soc.* **143**, 2173–2177 (2021).
20. Wang, Y. et al. Catalysis with two-dimensional materials confining single atoms: concept, design, and applications. *Chem. Rev.* **119**, 1806–1854 (2019).
21. Peng, P. et al. A pyrolysis-free path toward superiorly catalytic nitrogen-coordinated single atom. *Sci. Adv.* **5**, aaw2322 (2019).
22. Wang, L. et al. A sulfur-tethering synthesis strategy toward high-loading atomically dispersed noble metal catalysts. *Sci. Adv.* **5**, eaax6322 (2019).
23. Chen, G. et al. Highly accessible and dense surface single metal FeN_4 active sites for promoting the oxygen reduction reaction. *Energy Environ. Sci.* **15**, 2619–2628 (2022).
24. Wan, X. et al. Fe–N–C electrocatalyst with dense active sites and efficient mass transport for high-performance proton exchange membrane fuel cells. *Nat. Catal.* **2**, 259–268 (2019).
25. Gu, J., Hsu, C. S., Bai, L., Chen, H. M. & Hu, X. Atomically dispersed Fe^{3+} sites catalyze efficient CO_2 electroreduction to CO. *Science* **364**, 1091–1094 (2019).
26. Li, Z. et al. Iridium single-atom catalyst on nitrogen-doped carbon for formic acid oxidation synthesized using a general host–guest strategy. *Nat. Chem.* **12**, 764–772 (2020).
27. Chen, W. et al. Deciphering the alternating synergy between interlayer Pt single-atom and NiFe layered double hydroxide for overall water splitting. *Energy Environ. Sci.* **14**, 6428–6440 (2021).
28. Zheng, T. et al. Copper-catalysed exclusive CO2 to pure formic acid conversion via single-atom alloying. *Nat. Nanotechnol.* **16**, 1386–1393 (2021).
29. Fei, H. et al. General synthesis and definitive structural identification of MN_4C_4 single-atom catalysts with tunable electrocatalytic activities. *Nat. Catal.* **1**, 63–72 (2018).
30. Feng, L., Wang, K. Y., Willman, J. & Zhou, H. C. Hierarchy in metal–organic frameworks. *ACS Cent. Sci.* **6**, 359–367 (2020).
31. Sorrenti, A. et al. Growing and shaping metal–organic framework single crystals at the millimeter scale. *J. Am. Chem. Soc.* **142**, 9372–9381 (2020).
32. Venna, S. R., Jasinski, J. B. & Carreon, M. A. Structural evolution of zeolitic imidazolate framework-8. *J. Am. Chem. Soc.* **132**, 18030–18033 (2010).
33. Shen, K. et al. Ordered macro-microporous metal-organic framework single crystals. *Science* **359**, 206–210 (2018).
34. Bai, Y. et al. Zr-based metal–organic frameworks: design, synthesis, structure, and applications. *Chem. Soc. Rev.* **45**, 2327–2367 (2016).
35. Kong, X. J. et al. Constructing new metal–organic frameworks with complicated ligands from 'one-pot' in situ reactions. *Chem. Sci.* **10**, 3949–3955 (2019).
36. Xing, L. et al. Top-down synthetic strategies toward single atoms on the rise. *Matter* **5**, 788–807 (2022).
37. Han, G. F. et al. Abrading bulk metal into single atoms. *Nat. Nanotechnol.* **17**, 403–407 (2022).
38. Yao, Y. et al. High temperature shockwave stabilized single atoms. *Nat. Nanotechnol.* **14**, 851–857 (2019).
39. Peng, Y. et al. Laser solid-phase synthesis of single-atom catalysts. *Light Sci. Appl.* **10**, 168 (2021).
40. Browne, M. P., Redondo, E. & Pumera, M. 3D printing for electrochemical energy applications. *Chem. Rev.* **120**, 2783–2810 (2020).
41. Lee, C. Y., Taylor, A. C., Nattestad, A., Beirne, S. & Wallace, G. G. 3D printing for electrocatalytic applications. *Joule* **3**, 1835–1849 (2019).

42. dos Santos, M. F. et al. 3D-printed low-cost spectroelectrochemical cell for in situ raman measurements. *Anal. Chem.* **91**, 10386–10389 (2019).
43. Yuk, H. et al. 3D printing of conducting polymers. *Nat. Commun.* **11**, 1604 (2020).
44. Hartings, M. R. & Ahmed, Z. Chemistry from 3D printed objects. *Nat. Rev. Chem.* **3**, 305–314 (2019).
45. Zhang, M. et al. Hierarchical-coassembly-enabled 3D-printing of homogeneous and heterogeneous covalent organic frameworks. *J. Am. Chem. Soc.* **141**, 5154–5158 (2019).
46. Hou, W. et al. Automatic generation of 3D-printed reactionware for chemical synthesis digitization using chemscad. *ACS Cent. Sci.* **7**, 212–218 (2021).
47. Sullivan, I. et al. 3D printed nickel–molybdenum-based electrocatalysts for hydrogen evolution at low overpotentials in a flow-through configuration. *ACS Appl. Mater. Interfaces* **13**, 20260–20268 (2021).
48. Wu, Z. Y. et al. Electrochemical ammonia synthesis via nitrate reduction on Fe single atom catalyst. *Nat. Commun.* **12**, 2870 (2021).
49. Funke, H., Chukalina, M. & Scheinost, A. C. A new FEFF-based wavelet for EXAFS data analysis. *J Synchrotron Radiat.* **14**, 426–432 (2007).
50. Funke, H., Scheinost, A. C. & Chukalina, M. Wavelet analysis of extended X-ray absorption fine structure data. *Phys. Rev. B* **71**, 094110 (2005).
51. Wang, Y. et al. Phthalocyanine precursors to construct atomically dispersed iron electrocatalysts. *ACS Catal.* **9**, 6252–6261 (2019).
52. Zhang, S. et al. Electrocatalytically active Fe-$(O\text{-}C_2)_4$ single-atom sites for efficient reduction of nitrogen to ammonia. *Angew. Chem. Int. Ed. Engl.* **59**, 13423–13429 (2020).
53. Wang, Y. et al. High-efficiency oxygen reduction to hydrogen peroxide catalyzed by nickel single-atom catalysts with tetradentate N_2O_2 coordination in a three-phase flow cell. *Angew. Chem. Int. Ed. Engl.* **59**, 13057–13062 (2020).
54. Li, Z. et al. Axial chlorine coordinated iron-nitrogen-carbon single-atom catalysts for efficient electrochemical CO_2 reduction. *Chem. Eng. J.* **430**, 132882 (2022).
55. Han, Y. et al. Electronic structure engineering to boost oxygen reduction activity by controlling the coordination of the central metal. *Energy Environ. Sci.* **11**, 2348–2352 (2018).
56. Liu, M. et al. Atomically-dispersed NiN_4–Cl active sites with axial Ni–Cl coordination for accelerating electrocatalytic hydrogen evolution. *J. Mater. Chem. A* **10**, 6007–6015 (2022).
57. Li, P., Jin, Z., Fang, Z. & Yu, G. A single-site iron catalyst with preoccupied active centers that achieves selective ammonia electrosynthesis from nitrate. *Energy Environ. Sci.* **14**, 3522–3531 (2021).
58. Singh, B. et al. Single-atom (iron-based) catalysts: synthesis and applications. *Chem. Rev.* **121**, 13620–13697 (2021).
59. Tang, J. et al. Injection-free delivery of MSC-derived extracellular vesicles for myocardial infarction therapeutics. *Adv. Healthcare Mater.* **11**, 2100312 (2022).
60. Ravel, B. & Newville, M. ATHENA, ARTEMIS, HEPHAESTUS: data analysis for X-ray absorption spectroscopy using IFEFFIT. *J. Synchrotron Radiat.* **12**, 537–541 (2005).
61. Li, L. et al. Efficient nitrogen fixation to ammonia through integration of plasma oxidation with electrocatalytic reduction. *Angew. Chem. Int. Ed. Engl.* **60**, 14131–14137 (2021).
62. Kresse, G. & Furthmuller, J. Efficient iterative schemes for ab initio total-energy calculations using a plane-wave basis set. *Phys. Rev. B* **54**, 11169–11186 (1996).
63. Perdew, J. P., Burke, K. & Ernzerhof, M. Generalized gradient approximation made simple. *Phys. Rev. Lett.* **77**, 3865–3868 (1996).
64. Kresse, G. & Joubert, D. From ultrasoft pseudopotentials to the projector augmented-wave method. *Phys. Rev. B* **59**, 1758–1775 (1999).
65. Nørskov, J. K. et al. Origin of the overpotential for oxygen reduction at a fuel-cell cathode. *J. Phys. Chem. B* **108**, 17886–17892 (2004).
66. Peterson, A. A., Abild-Pedersen, F., Studt, F., Rossmeisl, J. & Nørskov, J. K. How copper catalyzes the electroreduction of carbon dioxide into hydrocarbon fuels. *Energy Environ. Sci.* **3**, 1311–1315 (2010).
67. Wan, H., Bagger, A. & Rossmeisl, J. Electrochemical nitric oxide reduction on metal surfaces. *Angew. Chem. Int. Ed. Engl.* **60**, 21966–21972 (2021).
68. Calle-Vallejo, F., Huang, M., Henry, J. B., Koper, M. T. M. & Bandarenka, A. S. Theoretical design and experimental implementation of Ag/Au electrodes for the electrochemical reduction of nitrate. *Phys. Chem. Chem. Phys.* **15**, 3196–3202 (2013).

Acknowledgements

DFT computations within this work were supported by computational resources provided by the Australian Government through NCI under the National Computational Merit Allocation Scheme and the Phoenix High Performance Compute (HPC) Service at The University of Adelaide. This research was undertaken on the XAS and Soft X-ray beamlines at the Australian Synchrotron, part of ANSTO. F.X. thanks H. Jin, C. Tang, Y. Jiao, Y. Zheng, P. Wang and J. Shan from the school of CEAM, A. Slattery and S. Gilbert from Adelaide Microscopy at the University of Adelaide, and H. Yu from the University of South Australia for constructive suggestions and help. This study was supported by the Australian Research Council (grant Nos. FL170100154-S.Z.Q and DP220102596-S.Z.Q), the New Zealand Health Research Council (grant No. 19/779 to C.X.), the New Zealand Ministry for Business, Innovation and Employment (grant No. MBIE Science Whitinga Fellowship, MWF-UOO2103 to C.X.) and the National Heart Foundation of New Zealand (grant Nos. 1891, 1896 to C.X.).

Author contributions

F.X. and C.X. conceived the project. S.-Z.Q. supervised the project and whole studies. F.X. and C.X. performed the materials preparations with the assistance of J.T. and T.W. F.X. and D.Y. conducted the electrochemical measurements. X.Z. conducted the DFT calculations. F.X., B.J., T.L. and G.L. performed the physicochemical characterizations. F.X., C.X., X.Z., D.Y. and S.-Z.Q. wrote the manuscript. S.-Z.Q. revised the manuscript for submission.

Competing interests

The authors declare no competing interests.

Additional information

Supplementary information The online version contains supplementary material available at https://doi.org/10.1038/s44160-022-00193-3.

Correspondence and requests for materials should be addressed to Shi-Zhang Qiao.

Peer review information *Nature Synthesis* thanks Yu Chen, Xiong Wen (David) Lou and the other, anonymous, reviewer(s) for their contribution to the peer review of this work. Primary Handling Editor: Alexandra Groves, in collaboration with the *Nature Synthesis* team.